

Hysteresis-Free Planar Perovskite Solar Module with 19.1% Efficiency by Interfacial Defects Passivation

Luigi Vesce, Maurizio Stefanelli, Luigi A. Castriotta, Afshin Hadipour, Stijn Lammar, Bowen Yang, Jiajia Suo, Tom Aernouts, Anders Hagfeldt, and Aldo Di Carlo*

In few years, perovskite solar devices have reached high efficiency on lab scale cells. Upscaling to module size, effective perovskite recipe and posttreatment are of paramount importance to the breakthrough of the technology. Herein this work, the development of a low-temperature planar n-i-p perovskite module (11 cm² aperture area, 91% geometrical fill factor) is reported on, exploiting the defect passivation strategy to achieve an efficiency of 19.1% (2% losses stabilized) with near-zero hysteresis, that is the most unsolved issue in the perovskite photovoltaic technology. The I/Br (iodine/bromide) halide ion ratio of the triplecation perovskite formulation and deposition procedure are optimized to move from small area to module device and to avoid the detrimental effect of dimethyl sulfoxide (DMSO) solvent. The organic halide salt phenethylammonium iodide (PEAI) is adopted as surface passivation material on module size to suppress perovskite defects. Finally, homogeneous and defect-free layers from cell to module with only 8% relative efficiency losses, high reproducibility, and optimized interconnections are scaled by laser ablation methods. The homogeneity of the perovskite layers and of the full stack was assessed by optical, morphological, and light beam-induced current (LBIC) mapping characterizations.

The efficiency transfer from laboratory cells to module devices is of paramount importance to exploit at market level the PVSK PV technology. The uniformity of the deposition and the losses induced by front contact and cell interconnections are the main obstacles for scaling up the cell to a module level.^[7] The module design and the interconnection patterning can face and limit these issues. The losses related to layers' inhomogeneity are related to the difficulties in transferring to module devices deposition processes and material compositions optimized for the small area cells.^[8] In this context, the polycrystalline nature of solution-processed PVSK layers induces defects, such as at grain boundaries and vacancies during the fabrication process.^[9]

A PVSK-based solar device can be realized according to two categories related to the position and deposition order of electron-transporting material (ETM) and hole-transporting material (HTM).^[10,11]

When the ETM layer is deposited first, the device is fabricated in the n-i-p (direct) structure; when the HTM layer is deposited first, the device is fabricated in the p-i-n (inverted) structure. The direct structure comes from the dye-sensitized solar cell (DSSC) technology, while the inverted one from the organic solar cell.^[12]


The efforts devoted to scale up to the module level of the PSC led to the identification of different strategies able to maximize the efficiency for both the inverted p-i-n and direct n-i-p module architectures. In the first case, Deng et al. reported MAPBI₃

1. Introduction

Owing to their unique physical-chemical properties,^[1,2] organometal halide perovskites (PVSKs) permitted to develop a solution process photovoltaic (PV) technology able to deliver power conversion efficiencies higher than any thin-film PV and closely resembling the one of silicon.^[3] Thanks to a fine tuning of material compositions, device architectures and fabrication processes the efficiency of PVSK solar cells (PSCs) reached 25.5% for the single junction and 29.8% when used in tandem with silicon.^[3-6]

L. Vesce, M. Stefanelli, L. A. Castriotta, A. Di Carlo
CHOSE – Centre for Hybrid and Organic Solar Energy
Department of Electronic Engineering
University of Rome “Tor Vergata”
Via del Politecnico 1, 00133 Rome, Italy
E-mail: aldo.dicarlo@uniroma2.it

A. Hadipour, S. Lammar, T. Aernouts
IMEC
Thin-Film PV
IMEC – Partner in EnergyVille and Solliance
Thor Park 8320, 3600 Genk, Belgium

 The ORCID identification number(s) for the author(s) of this article can be found under <https://doi.org/10.1002/solr.202101095>.

DOI: 10.1002/solr.202101095

B. Yang, J. Suo, A. Hagfeldt
Laboratory of Photomolecular Science
Institute of Chemical Sciences and Engineering
School of Basic Sciences
Ecole Polytechnique Fédérale de Lausanne
CH-1015 Lausanne, Switzerland

B. Yang, J. Suo, A. Hagfeldt
Department of Chemistry - Ångström Laboratory
Uppsala University
Box 523, SE-751 20 Uppsala, Sweden

A. Di Carlo
ISM-CNR
Istituto di Struttura della Materia
Consiglio Nazionale delle Ricerche
via del Fosso del Cavaliere 100, 00133 Rome, Italy

PVSK films with reduced annealing time maintaining the stoichiometric composition and promoting a spontaneous de-doping process.^[13] The module, with an active area of 19.92 cm², uses poly(triaryl amine) (PTAA) as hole-transporting layer (HTL) and C₆₀/Bathocuproine (BCP) as electron-transporting layer (ETL). The efficiencies on active area were 19.1% and 19.03% for reverse and forward scans, respectively. Recently, the same group showed a formamidinium-caesium PVSK by compensating iodide vacancies and suppressing ion migration with an efficiency on active area (27 cm²) of 20.2% (18.6% stabilized).^[14] Chen et al. reached 20.1% PCE on 16.4 cm² active area by partially replacing dimethyl sulfoxide (DMSO) with solid-state carbonylhydrazide in MAFAPI PVSK. In the latter works, no PCEs in forward scan are reported.^[15] Concerning the n-i-p module, Xu et al. fabricated a TiO₂-based planar triple-cation solar module (fluorinated tin oxide [FTO]/TiO₂/CsMAFAPbI₃/Spiro-OMeTAD/Au) combining series and parallel cell connections.^[16] The maximum efficiency on active area was 18.82% (16.36%) for reverse (forward) scan, exhibiting a huge hysteresis with a hysteresis index (HI) = 1.15, defined as the relationship between the reverse and forward scan efficiencies. The scaling-up loss from cell to module is about 14%, mainly due to the drop of current and fill factor related to layer inhomogeneity losses.^[17] Bu et al. obtained high-quality formamidinium (FA)-based PVSK by forming a stable PbI₂•NMP (N-methylpyrrolidone) adduct that inhibits the formation of a solvent-coordinated PVSK intermediate complex.^[18] The double cation solar module (FTO/SnO₂/CsFAPbI₃/2D-PVSK/Spiro-OMeTAD/Au) has an efficiency of 19.3% (reverse scan) on 17.1 cm² active area. Du et al. developed an ionic liquid to passivate the CsMAFA PVSK surface defects.^[19] The efficiency on 10.2 cm² active area is 17% and 18.6% for reverse and forward scans, respectively. Recently, Liu et al. demonstrated that *o*-PDEAI₂ is an effective passivation agent to reach 21.4% efficient PVSK solar module.^[20] Here, the efficiency loss from small area cell to module device is more than 10% and no efficiency in forward scan is reported. Since the reported literature lacks device statistics, it is hard to appreciate the variation of the results.

From this short overview of the literature results, it appears clear that so far only some reports presented both reverse/forward scan and the related HI. Among the n-i-p-based devices, the hysteresis analysis, if present, revealed a huge discrepancy between the efficiency in reverse and forward (HI > 1.1). The current density–voltage *J*-*V* hysteresis is the most debatable and unsolved issue in PSC technology.^[21–24] Several reasons can explain hysteresis in PSC: ferroelectric property of the PVSK

layer; unbalanced charge-carrier transport related to the hole transport layer and the electron transport layers; ion migration; trapping/detrapping of charge carriers. The hysteretic behavior of PVSK-based devices is still one of the obstacles in the commercialization of the PVSK technology. Moreover, during the fabrication process, many defects trap states and grain boundaries can occur.^[25–27] Since in any kind of solar cell, defects are mainly localized at the surface/interface,^[28,29] the PVSK surface passivation is one of the most efficient method to suppress nonradiative recombination losses and to improve charge-carrier extraction and photovoltage, by forming a shielding layer.^[6,26,27] Recently, the use of organic halide salt phenethylammonium iodide (PEAI) resulted to be more effective than 2D PEA₂PbI₄ PVSK on top of a 3D PVSK.^[30,31]

In this work, by performing a judicious design of module and related interconnections with the transfer length method (TLM), exploiting interfacial defects PEA₁ passivation at module level (first time in literature) and optimizing the deposition to avoid the detrimental effect of DMSO solvent, we report highly efficient n-i-p modules (10 cm² active area with 90% aspect ratio, reproducibility with 2% error) able to achieve an efficiency of 19.1% (reverse scan)—18.5% (forward scan) with a very low HI (HI = 1.03). Since DMSO trapping during the film formation is a crucial point, as recently demonstrated,^[15] we developed a deposition procedure to avoid DMSO solvent sticking on to the device. Moreover, the scaling-up losses have been reduced to only 8% (small area cell efficiency is 20.7%) by optimizing an iodine-rich triple-cation composition and the related deposition procedures, and showing the good passivation of defects, the optimal layer homogeneity on large area devices that influences the module short-circuit current density (*J*_{sc}), and the optimized patterning process by laser technique. We demonstrated the quality and the defects-free layers by materials and device characterization.

2. Results and Discussion

2.1. From Cells to Modules

We adopted the SnO₂ (tin oxide) as ETL, a triple-cation composition based on an optimized I/Br (iodine/bromide) halide ion ratio as PVSK formulation, PEA₁ as passivation agent, and Spiro-OMeTAD as HTL (**Figure 1**) (see Experimental Section).^[27,32]

On cell size (0.09 cm²), this architecture produced an efficiency equal to 20.66% (20.72%) in reverse (forward) scan (HI = 1.00) at 1 sun illumination (**Figure 2a**).

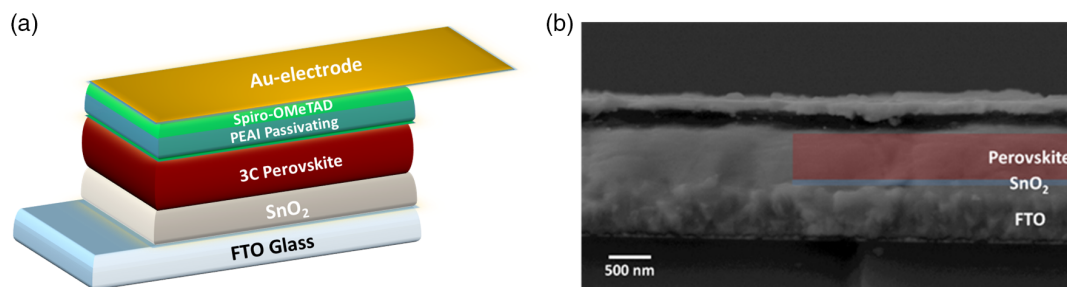


Figure 1. a) Perovskite (PVSK) device stack and b) scanning electron microscope (SEM) cross section.

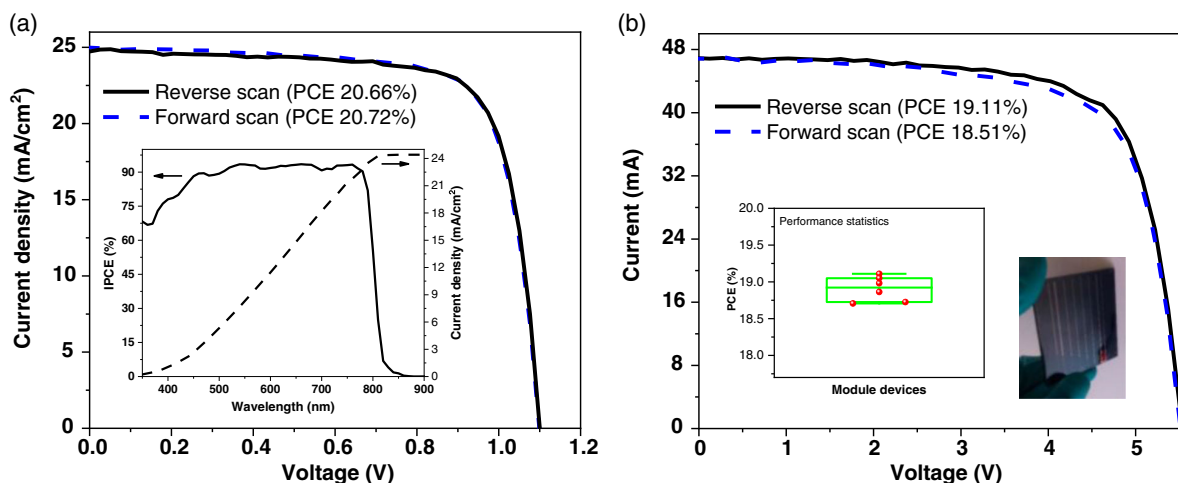


Figure 2. a) Small area cell (0.09 cm^2) current density/voltage plot in reverse and forward scans (1 SUN illumination, Class A Sun Simulator). Incident photon-to-electron conversion efficiency (IPCE) inset figure to validate the measured current density. b) Module device (10 cm^2 active area) current/voltage plot in reverse and forward scans. Efficiency statistics inset figure of six fabricated modules.

The high current density (24.77 mA cm^{-2}) is confirmed by the integrated current density from incident photon-to-electron conversion efficiency (IPCE) (Figure 2a). The spin-coating deposition method and the layer sequence of small cell are then used for scaling up to module size (10 cm^2 active area, 11 cm^2 aperture area, and 91% geometrical fill factor). Spin-coating methods are commonly used in large-scale industrial scenarios such as coatings, nanoelectronics, displays, bio-industries, and digital versatile disc.^[33–38] In particular, spin-coating is still a favorable technique not only for conventional silicon PVs but also for emerging ones such as copper zinc tin sulfide (CZTS).^[39,40] Moreover, since the dimensions of the silicon wafers, c-Si/PSC tandem technology can adopt the spin-coating technique.^[41] To scale up to module size, we have optimized the PVSK composition, and the spin-coating ramping, speed, and timing (see Experimental Section) for both PVSK solution and antisolvent, since the material composition and deposition parameters optimized for small-area cells induced cracks, inhomogeneous layer, pinholes, agglomeration sites, and amorphous PVSK phase when scaled to module size (Figure S1, S2, Supporting Information). First, we experimented that a PbI_2 excess and a different *N,N*-dimethylformamide/dimethyl sulfoxide (DMF/DMSO) ratio from the one adopted did not guarantee a homogeneous coverage (Figure S2, Supporting Information) of the 32 cm^2 substrate as in the small area substrate (6.25 cm^2) adopted for the lab scale cell present in literature. The spin-coating parameters for the small area cell (2000 rpm, 9 s ramp up, 10 s + 6000 rpm, 2 s ramp up, 28 s; 600 μL chlorobenzene 15 s before end) do not guarantee a uniform and defects-free coverage because the initial “10 s” at 2000 rpm delays the antisolvent dripping causing cracks in the final film.^[27] Moreover, by adding the antisolvent at 6000 rpm, the antisolvent is removed so fast by the spin speed that DMSO solvent is not completely washed out. To overcome these problems, we developed a specific and optimized spin-coating procedure: the PVSK solution is deposited at 2000 rpm with 10 s ramp up to fully cover the substrate but without persisting at this speed to avoid DMSO sticking on to the substrate. This is a

very crucial point, because DMSO was trapped during film formation and formed voids at PVSK-substrate interface, as it has been recently demonstrated for a different p–i–n architecture.^[15] After 10 s at 6000 rpm to reduce the thickness, the spin-coater slows down to 3000 rpm to permit the antisolvent dripping just before ramping up to 6000 rpm. After the antisolvent dripping, if the spin-coater is still at 3000 rpm, chlorobenzene cannot be quickly removed after DMSO washing and will damage the PVSK surface. The amount of chlorobenzene is 5 times more than the small area case because of the module size. Moreover, to avoid cracks on the PVSK film, it is very crucial that the velocity of the antisolvent dripping and the distance between substrate and pipet tip.

The uniformity of the PVSK film was assessed by UV–vis and scanning electron microscope (SEM)/profilometer investigation of the PVSK layer. The absorbance spectra in the investigated points are quite similar (Figure S3, Supporting Information), showing a good uniformity of the PVSK deposition. The PVSK layer, deposited by using the small area cell deposition parameters, shows an absorbance spectrum lower with respect to the best PVSK layer, with poor homogeneity in different spots (Figure S3, Supporting Information). The PVSK thickness was measured on 8 control points via profilometry, and in some spots, cross sections were investigated with SEM (Figure 1b). The measured thickness was $520 \pm 40 \text{ nm}$ with a $\approx 13 \text{ nm}$ roughness. The spatial uniformity of the full stack and the low presence of defects are confirmed by light beam-induced current (LBIC) measurements (Figure 3a).^[42]

The map shows a high level of homogeneity (no huge local defects or currents gradients) of all the layers involved in the cell stack (ETL/PVSK/PEAI/HTL). The standard deviation associated to the normal dispersion of the LBIC data is equal to 5.6%.

The improved deposition strategy, PEAi passivation (see section 2.2), and cells’ interconnection (see Section 2.3) resulted in a max module efficiency on active area of 19.11% (18.51%) in reverse (forward) scan with an efficiency reduction of only 8% with respect to the small area cell, low HI (HI = 1.03)

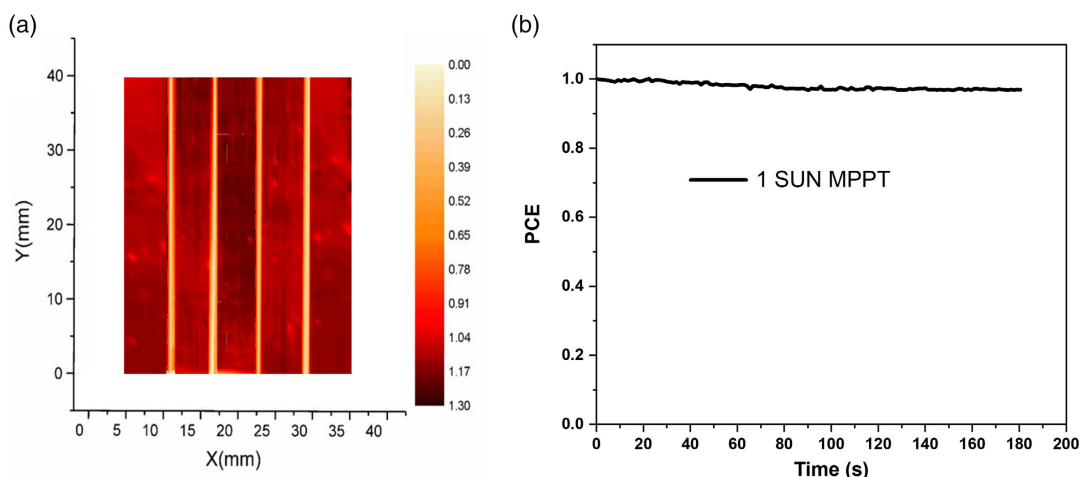


Figure 3. a) Light beam-induced current (LBIC) map of the PVSK planar module. The standard deviation associated to the normal dispersion of the LBIC data is equal to 5.6%. b) maximum power point tracking (MPPT) at 1 SUN of the fabricated PVSK module.

(Figure 2b), and 2% losses at 1 SUN maximum power point tracking (MPPT) (Figure 3b). Inset in Figure 1b shows the high reproducibility of six fabricated modules (less than 2% error).

2.2. PEAI Passivation

We performed X-Ray diffraction (XRD) on PVSK films with and without PEAI passivation agent to prove the presence of the PEAI on the 3D PVSK surface (Figure 4a).

The diffraction peaks for the PVSK layers with and without PEAI are the same except for a new diffraction peak at about 4.7° that is related to the PEAI crystal itself, as reported in literature.^[30] Moreover, since we have not performed any annealing after the PEAI deposition, no diffraction peak at 5.4° is visible that corresponds to the 2D PVSK PEA_2PbI_4 .^[30,31,43,44] In this work, we chose the more effective way of passivating the 3D PVSK with PEAI interlayer as proved by literature.^[27,30] The beneficial effect of the optimized PVSK (Figure S1, Supporting

Information) and passivation layer is proved by the photoluminescence (PL) intensity increasing with respect to the unoptimized PVSK (Figure 4b). The reason behind this PL enhancement is related to the decrease of the recombination in the PVSK layer,^[27,45] since PEAI treatment suppresses the surface non-radiative recombination defects.^[30] Moreover, in Figure 3b, the PL curve related to the dark-yellowish unoptimized PVSK layer has a redshift. This particular PVSK layer has regions with dark-yellowish color respect to the black-reddish of the optimized layer. Wu et al. reported how different color regions exhibit different PL properties.^[46] In our case, the peak shift is related to an incomplete conversion of PbI_2 films into $\text{CH}_3\text{NH}_3\text{PbI}_3$ PVSK.

2.3. Laser Patterning Design

In the upscale process, the P2–P3 ablation steps by a laser source (here neodymium-doped yttrium orthovanadate (Nd:YVO_4)) are

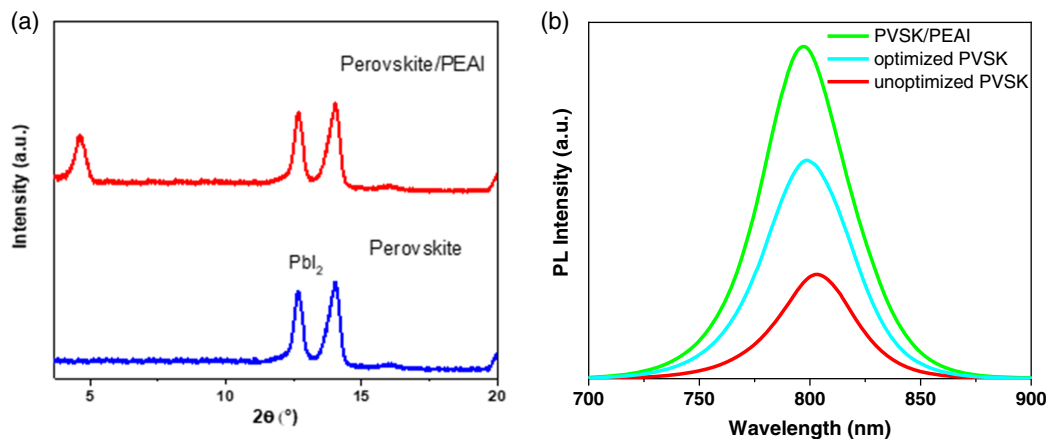


Figure 4. a) X-Ray diffraction (XRD) patterns of PVSK films before and after phenethylammonium iodide (PEAI) treatment. b) Photoluminescence (PL) of PVSK layer prior to the upscaling optimization. After the upscaling PVSK optimization and optimizing PVSK with the PEAI-passivating agent.

crucial to obtain low losses. The P2 (Experimental Section) removes the full stack (ETL/PVSK/PEAI/HTL) deposited on FTO from the vertical connection areas to series connect two adjacent cells with the subsequent electrode deposition. The realization of several laser areas with different fluences and number of pulses is useful to evaluate the laser ablation threshold of a material that is a heterogeneous stack. The main constrain is to avoid the transparent conductive oxide (TCO) damaging to limit the contact resistance (ρ_C) between the Au counter-electrode and the TCO. We analyzed the FTO sheet resistance (7 ohm sq.^{-1}), the stack thickness (800 nm), and the transfer length measurement (TLM) to minimize possible losses due to the laser process. A set of laser fluences (Figure 5a) has been considered and used on top of a full stack sample with glass/FTO/SnO₂/PVSK/PEAI/Spiro-OMeTAD.

Each specific etching line, corresponding to a given laser fluence, has been analyzed with a confocal microscope to assess the morphology of the etching. As a result of this analysis, we have chosen three different fluences capable of etching part of the stack without etching and cracking the underneath FTO. For each of the selected laser fluence we performed a full P2 process, repeating the etching line varying the raster scanning distance (RSD) to reach the full P2 width. In Figure 5b, it is shown one of the optimized square-shaped pads. Finally, those pads have been analyzed by profilometer (Figure 5c) to check the etching depth. Electrical measurements have been performed to evaluate the resistivity along the line (pad width is 1 mm to simplify the measurements). Finally, a fluence of 230 mJ cm^{-2} with $2 \mu\text{m}$ RSD permits to obtain a full stack removal (i.e., profile thickness/etching depth comparable to the full stack) and, therefore, was chosen for the module laser process. Figure S4, Supporting Information, shows the top-view energy-dispersive X-Ray spectroscopy (EDX) elemental analysis of the P2 ablation. The images showed that Pb, I, C, and O have been reduced in the P2 area with respect to the area surrounding it. Sn signal is still strong because of the FTO layer.

To complete the optimization work on P2 process, we realized TLM, following the scheme in our recent work.^[47] The TLM is required to have a proper estimation of the resistive losses since the high aspect ratio of a thin-film contact (width of the contact over the thickness of layers) prevents a more direct

measurement.^[48] We can consider transfer length (L_T) as the length that the charges travel in the TCO before they are transferred to the contact, defined as the square root of the ratio between specific contact resistance (ρ_C) and the conductivity of the electrode sheet resistance (R_{sh}), as shown in Figure 6. There is no need to exceed L_T when optimizing P2 contact because the geometry of a metal over less conductive thin semiconductor is characterized by a high aspect ratio among the width of the contact and the thickness of the electrode, inducing the current to flow preferentially in one direction and transferring its charges exponentially with a characteristic L_T . We use L_T to calculate the efficacy of the P2 contact because of its geometrically more significant parameter than ρ_C . From L_T definition, we can express the total resistance (R_T) as shown in Figure 6, where W is the width perpendicular to the current flow of the contact and L is the distance between contacts. As we can see from the graph, the linear fit allows us to understand the general behavior of the P2 efficacy: P2 with the optimized fluence of 230 mJ cm^{-2} has a behavior similar to the reference contact of Au over FTO. From the TLM graph, the intersection between the linear fit and the distance corresponds to $-2L_T$. In this way, P2 L_T value is $0.0041 \pm 0.0005 \text{ cm}$, with only $0.0023 \pm 0.0006 \text{ cm}$ difference with FTO/Au contact reference of $0.0018 \pm 0.0005 \text{ cm}$. In this way, we can confirm the efficacy of the P2 done with fluence per pulse of 230 mJ cm^{-2} .

The counter-electrode is then patterned (P3) in different stripes to realize the so-called Z-connection (see Experimental Section). P3 process is performed to guarantee a top isolation from one cell to the adjacent one: in this case, by isolating top electrode, we are addressing the current into a specific path inside the module, following the so-called Z direction (from the bottom to the top of each cell and vice versa). The P3 scribe is challenging because the layers underneath the top metal electrode may be damaged by parasitic heating induced by the laser pulses.^[42] Nevertheless, it was possible to successfully transfer the P3 process for gold electrodes as developed in previous studies, obtaining good electrical insulation. We optimized the P3 process following a recently reported procedure based on a grid scheme.^[49] The dead area width is $600 \mu\text{m}$ for each interconnection (Figure S4, Supporting Information).

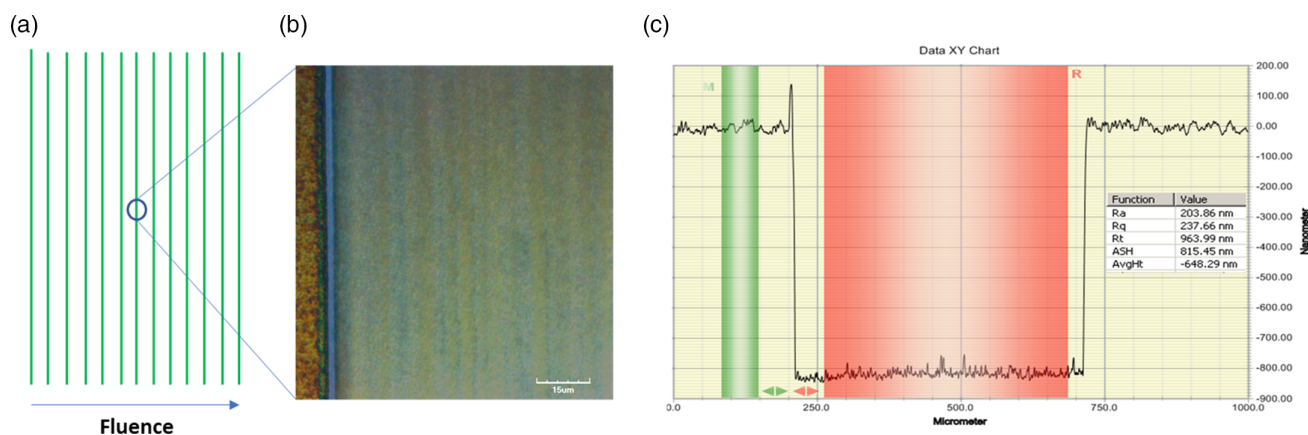


Figure 5. a) Single lines at different fluences; b) optimized laser-processed pad; and c) thickness check.

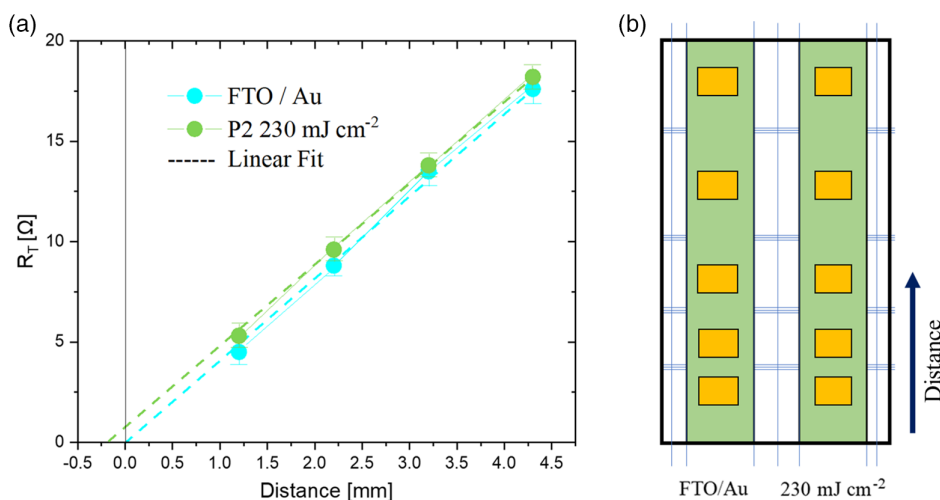


Figure 6. a) Transfer length measurement (TLM) plot; b) design of the samples used for TLM: blue lines represent P1 scribes, yellow pads represent the gold contact and green pads indicate the stripes used for TLM, using reference FTO/Au and 230 mJ cm⁻².

3. Conclusion

In conclusion, we presented the efforts to push module efficiency close to cell performance by improving structural design, material chemistry, and process (coating and laser ablation)^[50] with negligible hysteresis. PEAI passivation strategy was performed for the first time on a highly efficient module device and its presence was verified by XRD characterization. The scaling-up loss is about 8% and the maximum efficiency is 19.11% (18.51% in forward scan). The stabilized efficiency is more than 18.7% and the repeatability of the full process is lower than 2%. The reported simple and reproducible method represents an outstanding baseline to be transferred to large-area modules (size ≥ 100 cm²) by scalable full fabrication procedure out of glove box.^[7]

4. Experimental Section

Device Fabrication: The devices were composed by a 2.5 × 2.5 and 5.6 × 5.6 cm² FTO-covered glass (Pilkington, 7 Ω sq.⁻¹) to realize small area cells and modules, respectively. The fabrication procedure was equal for cells and modules except for the P2 and P3 laser ablation steps.

Substrate Preparation: FTO was patterned (P1) to form 5 series connected cells by a 15 ns Nd:YVO₄-pulsed UV laser system at 355 nm. The substrates were cleaned with a soap/water solution, then in an ultrasonic bath with acetone, ethanol, and 2-propanol for 10 min each and finally in a UV-ozone oven.

ETL and PVSK Layer: A SnO₂ solution in water (Alfa Aesar, 1:5 v/v) was stirred, sonicated, and filtered prior to the deposition step. The as-prepared solution was spin-coated (2800 rpm, 2 s ramp up, 60 s) on to the substrates and then annealed on a hot plate at 150 °C for 10 min in ambient air. We deposited by spin-coating technique in nitrogen air the triple-cation PVSK Cs_{0.05}FA_{0.85}MA_{0.10}Pb(I_{0.97}Br_{0.03})₃ in DMF/DMSO (0.76 mL/0.24 mL for 1 mL solution). The precursor solution and secondly chlorobenzene were spun on to the substrate. The spin-coating parameters for the small-area cell were 2000 rpm, 9 s ramp up, 10 s + 6000 rpm, 2 s ramp up, 28 s. The parameters for the module were 2000 rpm, 10 s ramp up, 0 s + 6000 rpm, 2 s ramp up, 10 s + 3000 rpm, 0 s ramp up, 5 s + 6000 rpm, 0 s ramp up, 13 s. In both cases, we added chlorobenzene

(600 μL and 3 mL) 15 s before end. After spin-coating, the PVSK was annealed at 120 °C for 20 min.

Passivation Layer and HTL: Dyenamo PEAI passivation material in isopropyl alcohol (3.74 mg mL⁻¹) and HTL Spiro-OMeTAD solution in chlorobenzene (95.1 mg mL⁻¹) doped with 4-tert-butylpyridine (TBP) (35.5 μL) and lithium bis(trifluoromethanesulfonyl)imide (Li-TFSI) (20.6 μL from a stock solution of 520 mg mL⁻¹) were spin-coated (PEAI at 2000 rpm, 0 s ramp up, 25 s; Spiro at 4000 rpm, 2 s ramp up, 20 s) on top of the PVSK layer subsequently.

P2 Laser Process: The next step was the removal (P2) by a Nd:YVO₄ raster 15 ns pulsed UV laser system at 355 nm (Explorer One HP 355-4, 50 μJ, 80 kHz) with a fluence of 230 mJ cm⁻² of the full stack (SnO₂/Cs_{0.05}FA_{0.85}MA_{0.10}Pb(I_{0.97}Br_{0.03})₃/PEAI/SpiroMeOTAD) deposited on FTO from the vertical connection areas to series connect two adjacent cells with the subsequent electrode deposition.

Top Electrode: Subsequently to the P2 process, 90 nm thick gold counter-electrode was thermally evaporated into a high vacuum chamber in nitrogen air. The counter-electrode was then patterned (P3) in different stripes by a raster 15 ns pulsed UV laser system at 355 nm with a fluence of 59 mJ cm⁻².

Device Characterization: The PV performance was measured with a class A sun simulator (Sun 2000, Abet) at air mass 1.5 1000 W m⁻² calibrated with an SKS 1110 sensor (Skye Instruments Ltd.); the system was equipped with a 2612 source meter (Keithley Instruments Inc.) and a LabVIEW interface. The IPCE equipment (Arkeo) was from Cicci Research. The absorbance and photoluminescence (PL) spectra were obtained with a UV-vis spectrometer (UV-2550, Shimadzu) and with a PL measurement system (Arkeo, Cicci Research), respectively. The film profiles were measured using a profilometer (DEKTA 150, Veeco Instruments Inc.). SEM images were acquired by VEGA 4 TESCAN Analytics machine at 15 keV. XRD measurements were carried out using a Siemens D5000 θ -2 θ goniometer with Cu K α ($\lambda = 1.54051$ Å) radiation and a 3° Soller slit collimator, S-3, which had a resolution of $2\theta = 0.01^\circ$ (Bruker AXS, Karlsruhe, Germany) at room temperature. The confocal microscope images were realized by Olympus OLS-4000 system. The LBIC characterization was realized by scanning the entire aperture area of the module and measuring the local photocurrent induced by the optical beam at 530 nm for each scan. An inverted microscope (DMI 5000, Leica) was coupled with a monochromator (Cornerstone 130) illuminated by a 200 W xenon lamp. The samples short-circuit photocurrent was detected by a phase-sensitive detection system composed by an optical chopper and two digital lock-in amplifiers (EG&G 7265).

Supporting Information

Supporting Information is available from the Wiley Online Library or from the author.

Acknowledgements

The authors were supported by the European Union's Horizon 2020 Framework Program for funding Research and Innovation under grant agreement nos. 764047 (ESPResSo) and 826013 (IMPRESSIVE). The authors acknowledge the project UNIQUE, supported under the umbrella of SOLAR-ERA.NET_cofund by ANR, PtJ, MUR (GA 775970), MINECOAEI, SWEA, within the European Union Framework Programme for Research and Innovation Horizon 2020 (Cofund ERANET Action, No. 691664).

Conflict of Interest

The authors declare no conflict of interest.

Data Availability Statement

The data that support the findings of this study are available from the corresponding author upon reasonable request.

Keywords

high efficiency, module upscaling, passivation, perovskite photovoltaics

Received: December 29, 2021

Revised: March 15, 2022

Published online: April 10, 2022

- [1] A. Kojima, K. Teshima, Y. Shirai, T. Miyasaka, *J. Am. Chem. Soc.* **2009**, *131*, 6050.
- [2] H. S. Kim, C. R. Lee, J. H. Im, K. B. Lee, T. Moehl, A. Marchioro, S. J. Moon, R. Humphry-Baker, J. H. Yum, J. E. Moser, M. Grätzel, N. G. Park, *Sci. Rep.* **2012**, *2*, 1.
- [3] NREL, *Best research-cell efficiency chart 2022*, <https://www.nrel.gov/pv/cell-efficiency.html> (accessed: February 2022).
- [4] H. J. Snaith, *Nat. Mater.* **2018**, *17*, 372.
- [5] M. A. Green, E. D. Dunlop, J. Hohl-Ebinger, M. Yoshita, N. Kopidakis, X. Hao, *Prog. Photovoltaics Res. Appl.* **2020**, *28*, 629.
- [6] J. J. Yoo, G. Seo, M. R. Chua, T. Gwan Park, Y. Lu, F. Rotermund, Y.-K. Kim, C. S. Moon, N. J. Jeon, J.-P. Correa-Baena, V. Bulović, S. S. Shin, M. G. Bawendi, J. Seo, *Nature* **2021**, *590*, 587.
- [7] L. Vesce, M. Stefanelli, J. P. Herterich, L. A. Castriotta, M. Kohlstädt, U. Würfel, A. Di Carlo, *Sol. RRL* **2021**, *5*, 1.
- [8] Z. Yang, C. C. Chueh, F. Zuo, J. H. Kim, P. W. Liang, A. K. Y. Jen, *Adv. Energy Mater.* **2015**, *5*, 1.
- [9] S. G. Motti, D. Meggiolaro, A. J. Barker, E. Mosconi, C. A. R. Perini, J. M. Ball, M. Gandini, M. Kim, F. De Angelis, A. Petrozza, *Nat. Photonics* **2019**, *13*, 532.
- [10] Z. Song, S. C. Watthage, A. B. Phillips, M. J. Heben, *J. Photonics Energy* **2016**, *6*, 022001.
- [11] N. K. Elumalai, M. A. Mahmud, D. Wang, A. Uddin, *Energies* **2016**, *9*, 861.
- [12] L. Meng, J. You, T. F. Guo, Y. Yang, *Acc. Chem. Res.* **2016**, *49*, 155.
- [13] Y. Deng, Z. Ni, A. F. Palmstrom, J. Zhao, S. Xu, C. H. Van Brackle, X. Xiao, K. Zhu, J. Huang, *Joule* **2020**, *4*, 1949.
- [14] Y. Deng, S. Xu, S. Chen, X. Xiao, J. Zhao, J. Huang, *Nat. Energy* **2021**, *6*, 633.
- [15] S. Chen, X. Dai, S. Xu, H. Jiao, L. Zhao, J. Huang, *Science* **2021**, *373*, 902.
- [16] Y. Xu, S. Wang, L. Gu, N. Yuan, J. Ding, *Sol. RRL* **2021**, *5*, 1.
- [17] L. A. Castriotta, F. Matteocci, L. Vesce, L. Cinà, A. Agresti, S. Pescetelli, A. Ronconi, M. Löffler, M. M. Stylianakis, F. Di Giacomo, P. Mariani, M. Stefanelli, E. M. Speller, A. Alfano, B. Paci, A. Generosi, F. Di Fonzo, A. Petrozza, B. Rellinghaus, E. Kymakis, A. Di Carlo, *ACS Appl. Mater. Interfaces* **2021**, *13*, 11741.
- [18] T. Bu, J. Li, H. Li, C. Tian, J. Su, G. Tong, L. K. Ono, C. Wang, Z. Lin, N. Chai, X. L. Zhang, J. Chang, J. Lu, J. Zhong, W. Huang, Y. Qi, Y. B. Cheng, F. Huang, *Science* **2021**, *372*, 1327.
- [19] M. Du, X. Zhu, L. Wang, H. Wang, J. Feng, X. Jiang, Y. Cao, Y. Sun, L. Duan, Y. Jiao, K. Wang, X. Ren, Z. Yan, S. Pang, S. Liu, *Adv. Mater.* **2020**, *32*, 1.
- [20] C. Liu, Y. Yang, K. Rakstys, A. Mahata, M. Franckevicius, E. Mosconi, R. Skackauskaite, B. Ding, K. G. Brooks, O. J. Usiobo, J.-N. Audinot, H. Kanda, S. Driukas, G. Kavaliauskaite, V. Gulbinas, M. Dessimoz, V. Getautis, F. De Angelis, Y. Ding, S. Dai, P. J. Dyson, M. K. Nazeeruddin, *Nat. Commun.* **2021**, *12*, 1.
- [21] J. Ren, Z. Kan, *Chapter 1: Origin of Hysteresis in Perovskite Solar Cells*, AIP Publishing LLC, Woodbury, Long Island, NY **2020**.
- [22] B. Chen, M. Yang, S. Priya, K. Zhu, *J. Phys. Chem. Lett.* **2016**, *7*, 905.
- [23] H. J. Snaith, A. Abate, J. M. Ball, G. E. Eperon, T. Leijtens, N. K. Noel, S. D. Stranks, J. T. W. Wang, K. Wojciechowski, W. Zhang, *J. Phys. Chem. Lett.* **2014**, *5*, 1511.
- [24] S. N. Habisreutinger, N. K. Noel, H. J. Snaith, *ACS Energy Lett.* **2018**, *3*, 2472.
- [25] M. Abdi-Jalebi, Z. Andaji-Garmaroudi, A. J. Pearson, G. Divitini, S. Cacovich, B. Philippe, H. Rensmo, C. Ducati, R. H. Friend, S. D. Stranks, *ACS Energy Lett.* **2018**, *3*, 2671.
- [26] J. Suo, B. Yang, A. Hagfeldt, *Energies* **2021**, *14*, 4836.
- [27] H. Zhu, Y. Liu, F. T. Eickemeyer, L. Pan, D. Ren, M. A. Ruiz-Preciado, B. Carlsen, B. Yang, X. Dong, Z. Wang, H. Liu, S. Wang, S. M. Zakeeruddin, A. Hagfeldt, M. I. Dar, X. Li, M. Grätzel, *Adv. Mater.* **2020**, *32*, 1.
- [28] X. Zheng, B. Chen, J. Dai, Y. Fang, Y. Bai, Y. Lin, H. Wei, X. C. Zeng, J. Huang, *Nat. Energy* **2017**, *2*, 17102.
- [29] K. Yoshikawa, H. Kawasaki, W. Yoshida, T. Irie, K. Konishi, K. Nakano, T. Uto, D. Adachi, M. Kanematsu, H. Uzu, K. Yamamoto, *Nat. Energy* **2017**, *2*, 17032.
- [30] Q. Jiang, Y. Zhao, X. Zhang, X. Yang, Y. Chen, Z. Chu, Q. Ye, X. Li, Z. Yin, J. You, *Nat. Photonics* **2019**, *13*, 460.
- [31] P. Chen, Y. Bai, S. Wang, M. Lyu, J. H. Yun, L. Wang, *Adv. Funct. Mater.* **2018**, *28*, 1.
- [32] M. Ozaki, Y. Ishikura, M. A. Truong, J. Liu, I. Okada, T. Tanabe, S. Sekimoto, T. Ohtsuki, Y. Murata, R. Murdey, A. Wakamiya, *J. Mater. Chem. A* **2019**, *7*, 16947.
- [33] R. G. Larson, T. J. Rehg, in *Liquid Film Coating: Scientific Principles And Their Technological Implications* (Eds.: S.F. Kistler, P.M. Schweizer), Springer, Netherlands, Dordrecht, **1997**, pp. 709–734.
- [34] K. Norrman, A. Ghanbari-Siahkali, N. B. Larsen, *Annu. Rep. Prog. Chem. Sect. C Phys. Chem.* **2005**, *101*, 174.
- [35] T. Ogi, L. B. Modesto-Lopez, F. Iskandar, K. Okuyama, *Colloids Surf. A Physicochem. Eng. Asp.* **2007**, *297*, 71.
- [36] P. He, J. Cao, H. Ding, X. Zhao, Z. Li, in *Synthesis, Modeling, and Characterization of 2D Materials, and Their Heterostructures* (Eds.: E.-H. Yang, D. Datta, J. Ding, G. Hader), Elsevier, Amsterdam **2020**, pp. 351–384.
- [37] K. Jp, K. Jp, G. Fujii, K. Jp, T. Isa, K. Jp, A. Chiba, J. L. Costellia, (12) *United States Patent*, **2011**.
- [38] V. S. Raghuvanshi, G. Garnier, *Front. Chem.* **2019**, *7*, 535.

- [39] A. E.-H. B. Kashyout, S. El-Hashash, J. El Nady, M. Fathy, K. Shoueir, A. Wageh, A. El-Dissouky, R. A. Rassoul, *ACS Omega* **2021**, *6*, 13077.
- [40] S. Engberg, F. Martinho, M. Gansukh, A. Protti, R. Kungas, E. Stamate, O. Hansen, S. Canulescu, J. Schou, *Sci. Rep.* **2020**, *10*, 20749.
- [41] S. Akhil, S. Akash, A. Pasha, B. Kulkarni, M. Jalalah, M. Alsaari, F. A. Harraz, R. G. Balakrishna, *Mater. Des.* **2021**, *211*, 110138.
- [42] F. Matteocci, L. Vesce, F. U. Kosasih, L. A. Castriotta, S. Cacovich, A. L. Palma, G. Divitini, C. Ducati, A. Di Carlo, *ACS Appl. Mater. Interfaces* **2019**, *11*, 25195.
- [43] Y. Cho, A. M. Soufiani, J. S. Yun, J. Kim, D. S. Lee, J. Seidel, X. Deng, M. A. Green, S. Huang, A. W. Y. Ho-Baillie, *Adv. Energy Mater.* **2018**, *8*, 1.
- [44] U. Gunes, E. Bag Celik, C. C. Akgul, M. Koc, M. Ameri, B. E. Uzuner, M. Ghasemi, M. C. Sahiner, İ. Yildiz, H. Z. Kaya, S. Yerci, G. Gunbas, *Adv. Funct. Mater.* **2021**, *31*, 1.
- [45] J. Chen, N. G. Park, *ACS Energy Lett.* **2020**, *5*, 2742.
- [46] Y. W. Zong, B.-L. Jian, H.-C. Hsu, *Opt. Mater. Express* **2019**, *9*, 1882.
- [47] F. Di Giacomo, L. A. Castriotta, F. U. Kosasih, D. Di Girolamo, C. Ducati, A. Di Carlo, *Micromachines* **2020**, *11*, 1.
- [48] D. K. Schroder, *Semiconductor Material and Device Characterization* **2005**, p. 61.
- [49] L. Vesce, M. Stefanelli, F. Matteocci, L. A. Castriotta, E. Lamanna, J. Herterich, F. Di Giacomo, M. Kohlstadt, U. Wurfel, A. Di Carlo, *12th AEIT Int. Annu. Conf. AEIT 2020*, IEEE, Catania, Italy **2020**.
- [50] J. Y. Kim, J. W. Lee, H. S. Jung, H. Shin, N. G. Park, *Chem. Rev.* **2020**, *120*, 7867.